RSC Advances

ROYAL SOCIETY OF CHEMISTRY

PAPER

View Article Online
View Journal | View Issue

Cite this: *RSC Adv.*, 2025, **15**, 815

Tuning surface hydrophilicity of a $BiVO_4$ photoanode through interface engineering for efficient PEC water splitting†

Shuangwei Yu, Chunrong Su, Zhehui Xiao, Yi Kuang, Xue Gong, Xiong He,* Jinghua Liu,* Qianqian Jin and Zijun Sun *

This study presents a novel approach to enhance photoelectrochemical (PEC) water oxidation by integrating cobalt phthalocyanine (CoPc) with bismuth vanadate (BVO) *via* a direct solvothermal method. The as-prepared BVO@CoPc photoanode demonstrated a photocurrent density of 4.0 mA cm^{-2} at 1.23 V *vs.* RHE, which is approximately 3.1 times greater than that of the unmodified BVO, and has superior stability. The incident photon-to-current conversion efficiency (IPCE) of the BVO@CoPc photoanode reaches an impressive value of 81%, accompanied by significant enhancements in charge injection efficiency. This excellent performance can be ascribed to the enhanced hydrophilicity with the BVO/CoPc interface engineering, which facilitates interfacial interaction between the electrode and electrolyte, accelerates photogenerated charge carrier transfer and separation. Furthermore, compared to the immersion and drop-casting methods, the BVO@CoPc-S composite photoanode prepared *via* the solvothermal method exhibits a significant improvement in interfacial contact and surface hydrophilicity. These findings highlight the potential of the strategy based on interfacial hydrophilicity modification to overcome key limitations in PEC water splitting, providing a pathway to more efficient and durable photoanode design.

Received 21st November 2024
Accepted 6th January 2025

DOI: 10.1039/d4ra08254k

rsc.li/rsc-advances

1. Introduction

With the rising demand for renewable energy sources and environmental concerns, photoelectrochemical (PEC) water splitting has gained prominence as a promising technology for converting solar energy into clean hydrogen fuel.[1–3] PEC water splitting is divided into the hydrogen evolution reaction (HER) and the oxygen evolution reaction (OER).[4,5] Among these, OER is the rate-limiting step due to its complex four-electron transfer process. Consequently, the exploration and design of efficient photoanode materials with the facilitated kinetics of water oxidation is critical for PEC water-splitting systems.[6,7] Bismuth vanadate (BVO) has gained attention as a potential photoanode material because of its appropriate bandgap, stability under alkaline conditions, and relatively low cost. However, it is still restricted by poor charge separation efficiency and slow surface reaction kinetics.[8–11]

A widely adopted strategy to improve the PEC performance of BVO is the integration of transition metal-based co-catalysts into the BVO photoanode. This approach effectively reduces the reaction energy barrier for water oxidation while simultaneously enhancing the reaction kinetics.[12–15] For example, Sun and co-workers discovered that Co doping successfully introduced oxygen vacancies into BVO as catalytically active sites, improving overall water-splitting activity.[16] Liu *et al.* constructed an S-type heterojunction (S-$BiVO_4$/WO_3), in which the internal electric field formed at the interface can induce a stepwise charge transfer mechanism, ultimately enhancing the water oxidation ability.[17] However, the slow water oxidation kinetics at the photoanode–electrolyte interface remain a key issue hindering further improvement of the PEC water splitting performance.

In this situation, molecular catalysts have emerged as promising materials for oxygen evolution catalysis (OEC) due to their well-defined active sites, which allow precise control over catalytic activity and selectivity. Their inherently high activity, originating from metal centers and ligands, combined with highly tunable molecular structures, renders them highly attractive for broader applications.[18] Among them, metal phthalocyanine (MPc)-based complexes can be synthesized and deposited on the surface of BVO to enhance PEC water splitting performance. As an example, Sun's group demonstrated that BVO/CoPc hybrid photoanodes, prepared *via* drop-coating, achieved a photocurrent density of 3.23 mA cm^{-2} at 1.23 V *vs.* RHE.[19] As well, Shen *et al.* developed $BiVO_4$ thin films loaded

School of Electronic Engineering, Guangxi Key Laboratory of Multidimensional Information Fusion for Intelligent Vehicles, Guangxi University of Science and Technology, Liuzhou 545000, China. E-mail: hexiong@gxust.edu.cn; liujinghua@gxust.edu.cn; sunzijun@gxust.edu.cn

† Electronic supplementary information (ESI) available. See DOI: https://doi.org/10.1039/d4ra08254k

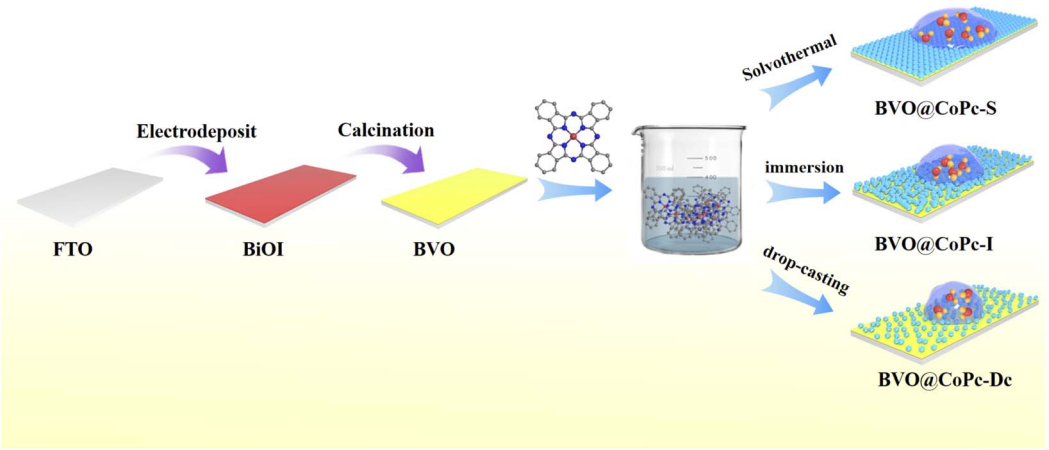

Scheme 1 Synthetic routes of BVO, BVO@CoPc-S, BVO@CoPc-I, and BVO@CoPc-Dc photoanodes.

with cobalt phthalocyanine ($CoPc(NH_2)_4/BiVO_4$), achieving a photocurrent density of 3.02 mA cm^{-2} under irradiation, attributed to the synergistic interaction between $CoPc(NH_2)_4$ and $BiVO_4$.[20] In similar studies, Zhao *et al.* employed a dipping method to co-assemble CuPc and FeOOH onto a $BiVO_4$ photoanode, achieving a photocurrent density of 3.67 mA cm^{-2} at 1.23 V *vs.* RHE.[21] The above discussion collectively highlight the effectiveness of $BiVO_4$/phthalocyanine complexes in significantly enhancing the PEC water splitting performance.

However, in these studies, the influence of interface contact between photoanode and electrolyte on water oxidation efficiency is rarely reported, the composite photoanode prepared with hydrophobic $BiVO_4$ and hydrophilic CoPc exhibited poor interfacial matching with the electrolyte. To accelerate water splitting, it is essential to rationally regulate hydrophilicity of the photoanode surface to improve the interfacial compatibility between the electrode and electrolyte. Recent researches have declared the interface engineering strategies with tuned hydrophilicity for enhanced PEC performance.[22,23] For instance, Wang's team enhanced the PEC performance of TiO_2 photoelectrode materials by improving interface properties through molecular monolayer modification. This chemical monolayer modification can change its wettability state, further inhibiting the recombination of electrons and holes.[24] Yue *et al.* adopted a convenient strategy to prepare super-hydrophilic H-CoAl-LDH/$BiVO_4$ composite photoanodes. The good surface wettability enables rapid adsorption of water molecules on plasma-engineered photoanodes with abundant active sites, achieving a photocurrent density of 3.5 mA cm^{-2} at 1.23 V *vs.* RHE, greatly boosting PEC water oxidation activity.[25] These findings underscore that hydrophilicity-based interfacial engineering is expected to further accelerate surface water oxidation reactions as a universal strategy.[26,27]

In this study, CoPc was introduced onto BVO electrode using three methods: solvothermal method (BVO@CoPc-S), impregnation method (BVO@CoPc-I), and drop coating method (BVO@CoPc-Dc), as shown in Scheme 1. The BVO@CoPc-S photoanode exhibited high surface hydrophilic properties and reached a photocurrent density of 4.0 mA cm^{-2} at 1.23 V *vs.* RHE, outperforming the BVO@CoPc-Dc and BVO@CoPc-I photoanodes at 1.43 and 1.38 times, respectively, and its stability was further reinforced. This enhancement is attributed to the BVO@CoPc-S's super-hydrophilic surface, which allows the electrolyte to penetrate the surface of the photoanode, increasing the effective contact area between the electrolyte and photoanode. Comprehensive physical characterization and kinetic tests revealed that surface wettability of the photoanode is a key to enhancing both the efficiency and stability of PEC water splitting.

2. Results and discussion

The BVO photoanode was fabricated according to a modified two-step process based on previously reported methods.[28] Then BVO@CoPc-S, BVO@CoPc-I, and BVO@CoPc-Dc were fabricated with different CoPc incorporation methods. Detailed preparation procedures for BVO@CoPc-S, BVO@CoPc-I, and BVO@CoPc-Dc photoanodes are provided in the ESI.† The morphology of these synthesized photoanodes (BVO, BVO@CoPc-Dc, BVO@CoPc-I, BVO@CoPc-S) were conducted using SEM. As illustrated in Fig. 1a, pure BVO presents a 3D worm-like structure, which facilitates electrolyte diffusion.[29] No significant morphological changes can be observed for BVO@CoPc-Dc, BVO@CoPc-I, and BVO@CoPc-S photoanodes as shown in Fig. 1b–d. Fig. 1e displays the energy dispersive X-ray (EDS) spectra of BVO@CoPc-S, indicating the presence of elements Bi, V, O, C, Co, and N. The Pt and Sn elements come from evaporation during the measurement and FTO glass, respectively. Transmission electron microscopy (TEM) and high-resolution transmission electron microscopy (HRTEM) images of the synthesized BVO@CoPc-S photoanodes are shown in Fig. 1f and g. The lattice spacing of 0.338 nm corresponding to the (112) plane of monoclinic BVO is observed in Fig. 1g.[30] In addition, there is a uniformly distributed amorphous layer, which is probably loaded with CoPc, tightly wrapped around the surface of BVO.[31] The high-quality interface between CoPc and BVO is anticipated to enhance charge transfer and boost PEC activity.

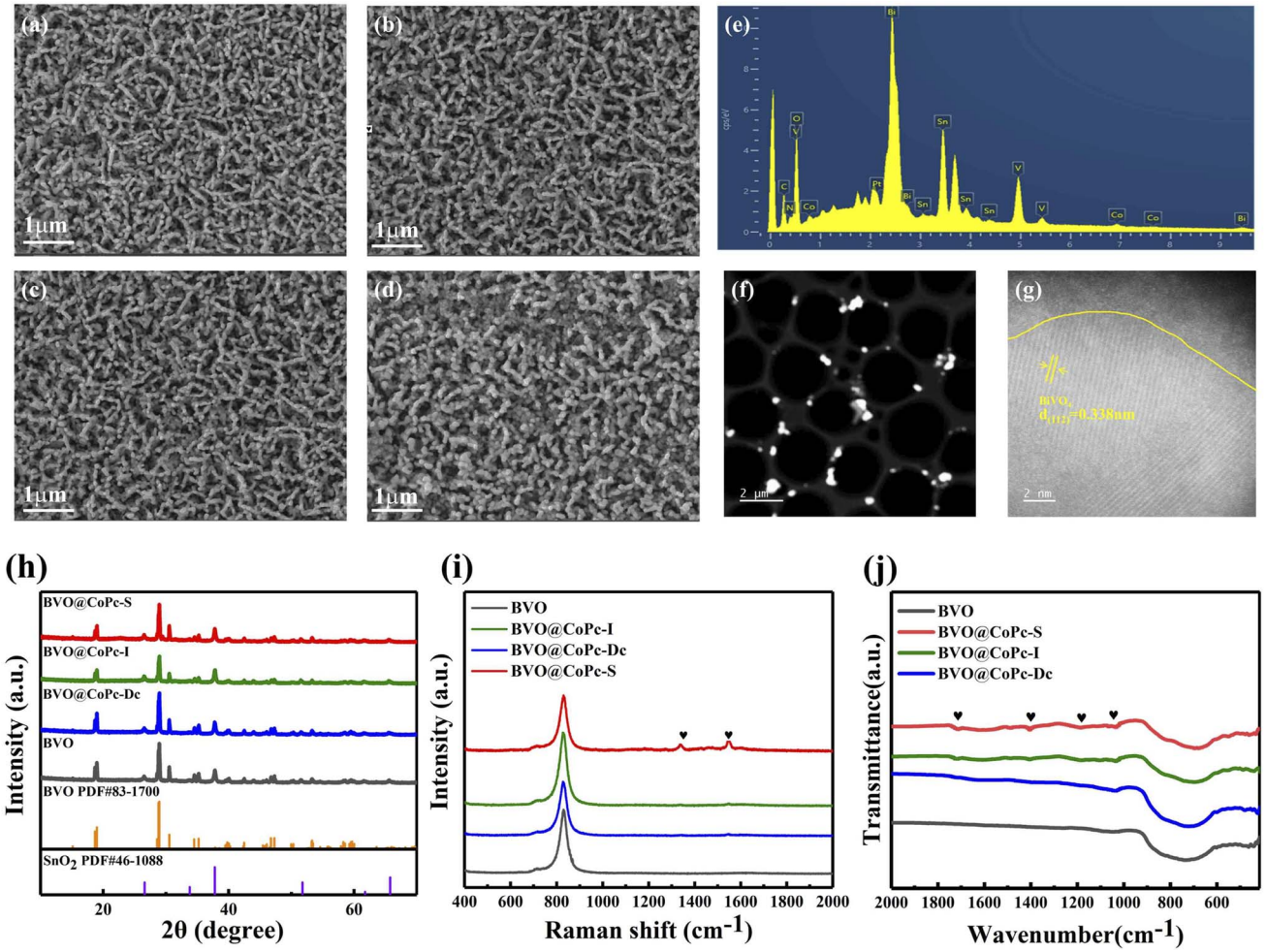

Fig. 1 (a–d) SEM images of the BVO, BVO@CoPc-Dc, BVO@CoPc-I, and BVO@CoPc-S photoanodes. (e) The EDS elemental mapping of BVO@CoPc-S photoanode. (f and g) TEM and HRTEM images of BVO@CoPc-S photoanode. (h–j) XRD patterns, Raman spectra, and FTIR spectra of these prepared photoanodes.

The XRD patterns of BVO, BVO@CoPc-Dc, BVO@CoPc-I and BVO@CoPc-S were shown in Fig. 1h. The characteristic diffraction peaks of these prepared photoanodes closely match those of monoclinic BVO (PDF#83-1700) and SnO_2 (PDF#46-1088), which confirms the successful synthesis of monoclinic BVO on fluorine-doped tin oxide substrates. However, no characteristic diffraction peaks corresponding to CoPc can be observed. The high dispersion or low loading of CoPc may be responsible for this phenomenon.[32] Fig. 1i exhibits the Raman spectra of these synthesized photoanodes. A distinct characteristic peak at 826 cm^{-1}, corresponding to V–O bonds BVO, can be detected. With CoPc incorporated in BVO, C–C stretching vibrational bands of the pyrrole group at 1138 cm^{-1} as well as C–N stretching vibrational bands of isoindoles at 1545 cm^{-1} were found.[33,34] This result proves the successful introduction of CoPc in BVO. Meanwhile, the intensity of these characteristic peaks is enhanced for BVO@CoPc-S. It suggests that the good integration of CoPc onto the BVO surface with the solvothermal method.

To further evaluate the CoPc decoration under different loading strategies, the FTIR spectra of these photoanodes were conducted as shown in Fig. 1j. An obvious absorption peak at 730 cm^{-1}, associated with V–O vibrations, can be observed. For BVO@CoPc-Dc, BVO@CoPc-I, and BVO@CoPc-S, new absorption peaks located around 1415 cm^{-1}, 1170 cm^{-1}, 1038 cm^{-1}, and 1720 cm^{-1} can be detected, which are attributed to the vibrations of the metal–ligand and phthalocyanine backbone, C=C bonding of the benzene ring in CoPc, and stretching vibration of the Pc ring, respectively.[35,36] Among these BVO@CoPc photoanodes, the BVO@CoPc-S photoanode exhibits the stronger intensity of these absorption peaks. Notably, for the BVO@CoPc-S photoanode, a slight blue shift of the V–O bond can be captured compared with pure BVO photoanode. These phenomena further indicate the successful synthesis of the BVO@CoPc-S photoanode as well as the strong chemical interactions between BVO and CoPc.[37] To further investigate the optical properties of these photoanodes, UV-Vis absorption spectra were conducted as shown in Fig. S1.† In agreement with previous reports, the absorption edge of bare BVO was observed

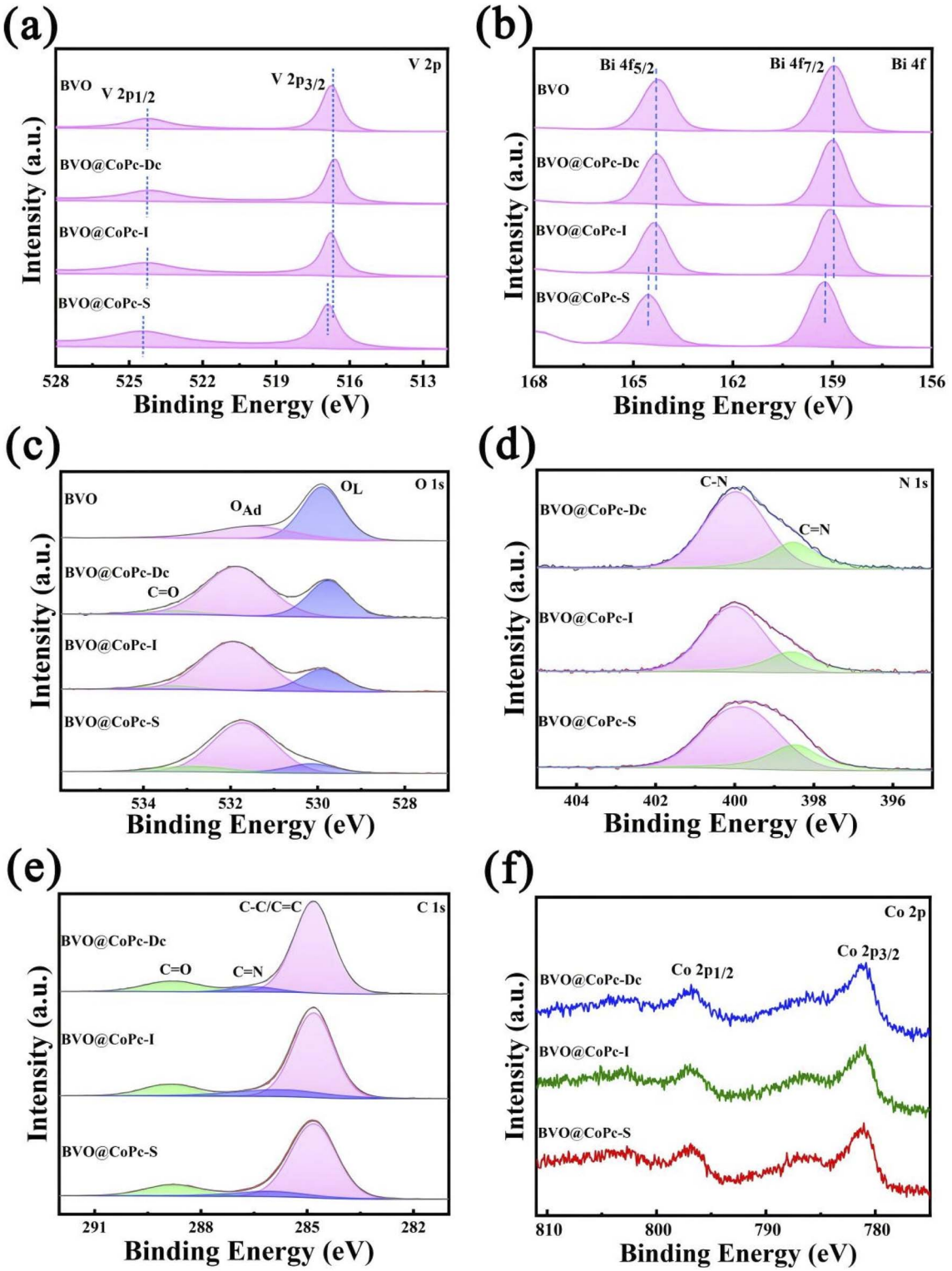

Fig. 2 XPS spectra of these prepared photoanodes. (a) V 2p, (b) Bi 4f, (c) O ls, (d) N ls, (e) C ls, and (f) Co 2p.

at 515 nm.[38] No obvious change can be observed for the absorption edge of these BVO@CoPc photoanodes. Meanwhile, two Q bands originated from CoPc appear at 605 and 690 nm, indicating the successful synthesis of BVO@CoPc photoanodes.[39]

X-ray photoelectron spectroscopy (XPS) was utilized to investigate the surface valence states and chemical composition of these photoanodes. The V 2p, Bi 4f, O 1s, N 1s, C 1s, and Co 2p XPS spectra are shown in Fig. 2. The V 2p XPS spectra (Fig. 2a) demonstrate the peaks located at 516.7 and 524.3 eV,

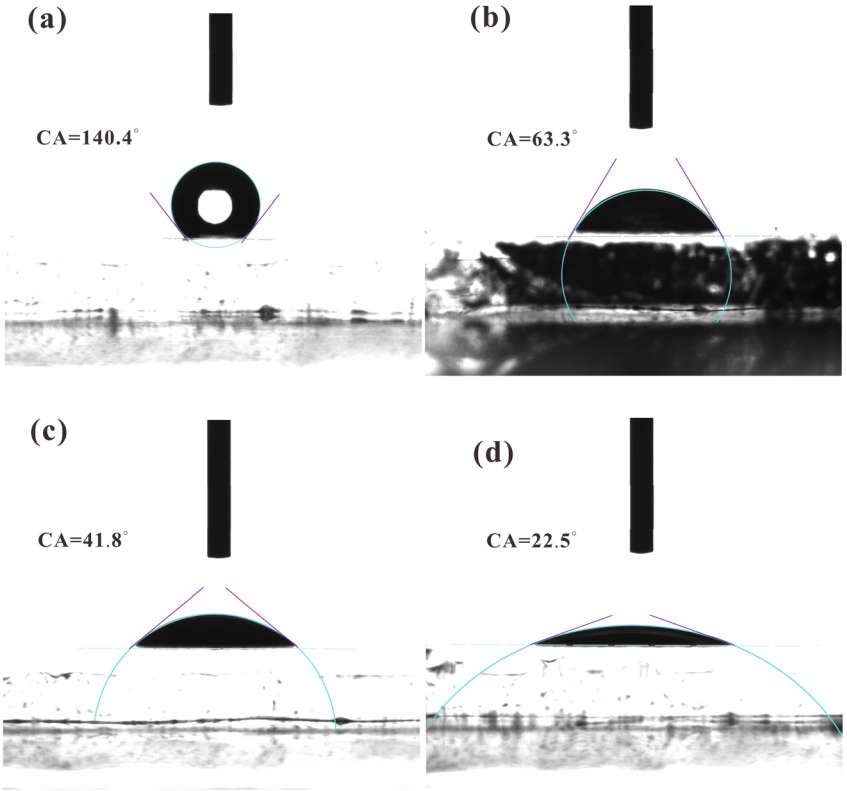

Fig. 3 Contact angle of (a) BVO, (b) BVO@CoPc-Dc, (c) BVO@CoPc-I and (d) BVO@CoPc-S photoanodes.

corresponding to V^{5+} $2p_{3/2}$ and V^{5+} $2p_{1/2}$, respectively. Peaks at 159.0 and 164.3 eV, assigned to Bi^{3+} $4f_{7/2}$ and Bi^{3+} $4f_{5/2}$, respectively, are seen in the Bi 4f spectra (Fig. 2b). It should be noted that the Bi 4f and V 2p XPS spectra of BVO, BVO@CoPc-Dc, and BVO@CoPc-I are similar, but a slight shift towards higher binding energy can be observed for Bi 4f and V 2p XPS spectra of BVO@CoPc-S. The Bi $4f_{7/2}$ and Bi $4f_{5/2}$ peaks are positively shifted to 159.3 and 164.6 eV, respectively. The peaks of V $2p_{1/2}$ and V $2p_{3/2}$ are shifted to 524.5 and 516.9 eV, respectively, indicating the strong chemical interaction between BVO and CoPc in BVO@CoPc-S.[20] This result is consistent with the findings from the FTIR analysis. For O 1s spectra (Fig. 2c), two distinct peaks are visible at 529.8 and 531.6 eV, corresponding to the lattice oxygen (O_L) and adsorbed oxygen (O_{Ad}), respectively. The hydroxyl groups of the adsorbed water molecules on the surface are responsible for the adsorbed oxygen, which can improve hydrophilicity.[40] For BVO@CoPc photoanodes, one new peak at 533.4 eV can be obtained, and assigned to C=O bonds in CoPc. The C=O bonds also could improve hydrophilicity and promote the absorption of dissolved oxygen on the surface.[41] These ratios of C=O, O_{Ad}, and O_L for these photoanodes were summarized in Table S1† based on O 1s XPS spectra. BVO@CoPc-S photoanode exhibits the highest O_{Ad} and C=O ratios, which lead to a more polar surface and more active water at the reaction site. Two distinct peaks at 398.5 and 400.0 eV, corresponding to C=C and C–N bonds, are present in the N 1s spectra (Fig. 2d). The C 1s spectrum (Fig. 2e) shows peaks at 284.8, 286.6, and 288.8 eV, which correspond to C–C/C=C, C=N, and C=O, respectively.[42] For Co 2p spectra (Fig. 2f), there are two characteristic peaks of Co $2p_{3/2}$ and Co $2p_{1/2}$ at 781.0, 796.7 eV for these BVO@CoPc photoanodes,[20] confirming the successful incorporation of CoPc into BVO.

To investigate the relationship between the surface wettability and CoPc loading strategy, the contact angles of these photoanodes were identified as shown in Fig. 3. The contact angle is a paramount index to the surface wettability of the photoanode. The contact angles of BVO, BVO@CoPc-Dc, BVO@CoPc-I, and BVO@CoPc-S are calculated as 140.4°, 63.3°, 41.4°, and 22.5°, respectively. The lower contact angle indicates the better hydrophilicity. Therefore, it can be concluded that incorporating CoPc significantly enhances the photoanode's hydrophilicity. Meanwhile, it can be obtained that BVO@CoPc-S possesses better hydrophilicity than other BVO@CoPc photoanodes. The improved hydrophilicity could promote electrolyte diffusion, accelerating the water oxidation kinetics with better contact between water molecules and active sites.[43]

The PEC performance of BVO, BVO@CoPc-Dc, BVO@CoPc-I, and BVO@CoPc-S photoanodes was performed using a conventional three-electrode system in 1 M KBi buffer electrolyte. As shown in Fig. 4a, BVO@CoPc-S photoanode demonstrates the highest photocurrent density of 4.0 mA cm^{-2} at 1.23 V *vs.* RHE, which is 3.11, 1.43 and 1.38 times that of BVO (1.32 mA cm^{-2}), BVO@CoPc-Dc (2.8 mA cm^{-2}) and BVO@CoPc-I (2.9 mA cm^{-2}), respectively. This outcome suggests that the incorporation of CoPc could improve the PEC performance. Additionally,

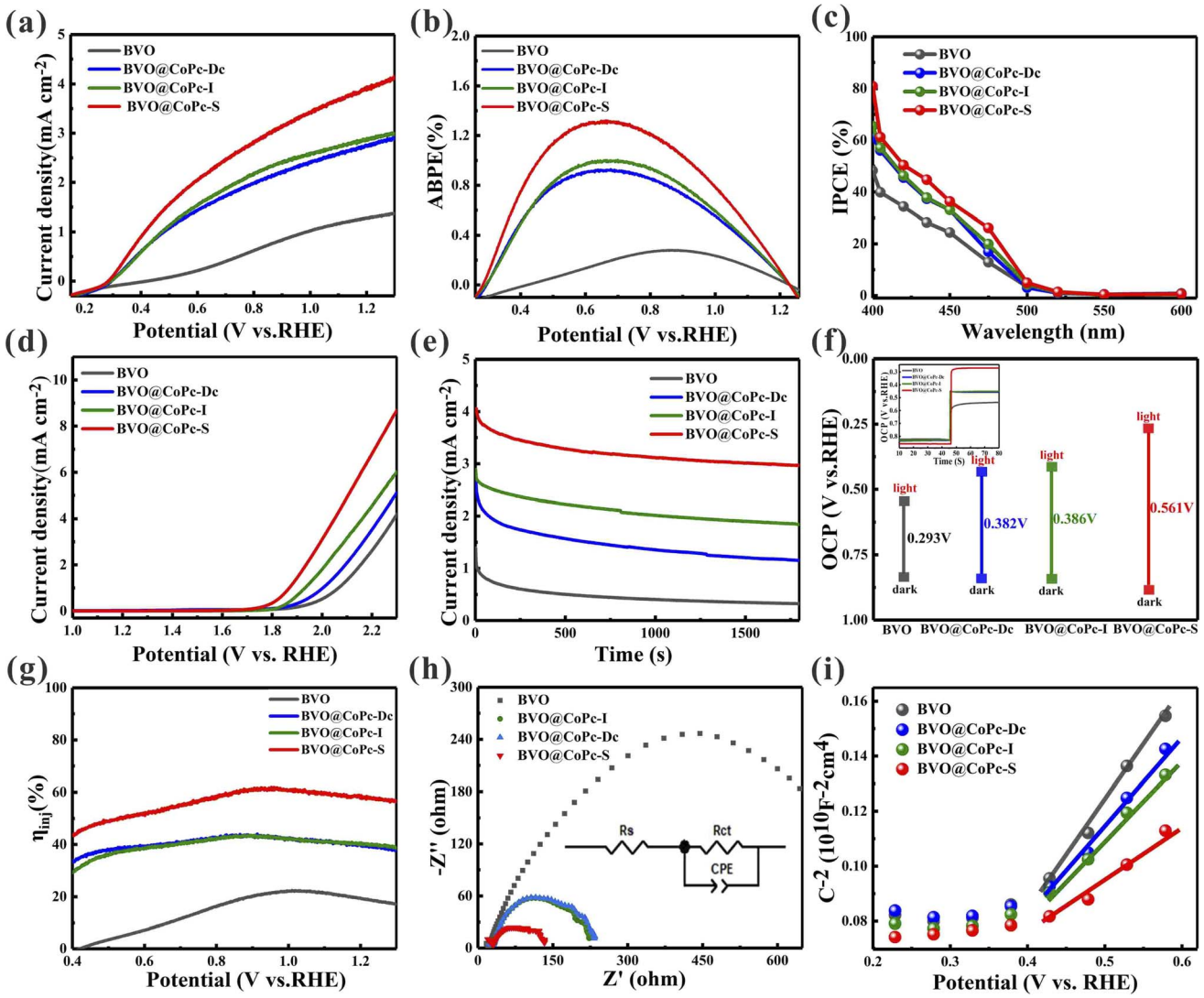

Fig. 4 (a) Linear scanning voltammetry (LSV), (b) ABPE, (c) IPCE, (d) LSV curves under dark, (e) stability curves, (f) open-circuit measurements, (g) charge injection efficiency, (h) EIS, and (i) Mott–Schottky plots of these prepared photoanodes.

BVO@CoPc-S photoanode exhibits optimal water oxidation which may be ascribed to better interface contact and hydrophilicity. The applied bias photon-to-current efficiency (ABPE) and the incident photon-to-current efficiency (IPCE) were conducted to evaluate the photoconversion efficiency of BVO, BVO@CoPc-Dc, BVO@CoPc-I, and BVO@CoPc-S photoanodes. As illustrated in Fig. 4b, compared with the maxima ABPE (0.28%) of the pristine BVO photoanode at 0.86 V_{RHE}, the maxima ABPE (0.92%) of the BVO@CoPc-Dc photoanode at 0.65 V_{RHE} and the maxima ABPE (1.01%) of the BVO@CoPc-Dc photoanode at 0.66 V_{RHE}, the maxima ABPE rises to 1.3% at 0.64 V_{RHE} for BVO@CoPc-S photoanode, indicating BVO@CoPc-S is conductive to the PEC water oxidation process. As can be seen in Fig. 4c, the IPCE of BVO@CoPc-S reaches 81% at 400 nm, which is higher than that of BVO (49%), BVO@CoPc-Dc (66%) and BVO@CoPc-I (67%). These analysis state that BVO@CoPc-S could effectively improve PEC performance with its unique interface contact and hydrophilicity. Linear Scanning Voltammetry (LSV) was used to measure oxygen evolution reaction (OER) curves under dark conditions. As shown in Fig. 4d, the BVO@CoPc-S photoanode has a lower overpotential than other photoanodes attributed to the rapid water oxidation kinetics with better hydrophilicity.

Fig. S2a† demonstrates the transient photocurrent response curves of BVO, BVO@CoPc-Dc, BVO@CoPc-I, and BVO@CoPc-S photoanodes. When the photoanodes are illuminated by light, an anodic photocurrent spike appears due to the production of photogenerated carriers (electrons and holes). With the recombination of photogenerated carriers, the photocurrent gradually decays, and ultimately reaches a steady state. For the quantitative analysis of the charge recombination process, the transient decay rate (D) was calculated with eqn (1), and the transient time constant (τ) could be determined when $\ln D = -1$.

$$D = \frac{I_t - I_{st}}{I_{in} - I_{st}} \quad (1)$$

Among these, the normalized parameter D is used to determine the electronic recombination behavior. I_t, I_{in}, and I_{st} are the

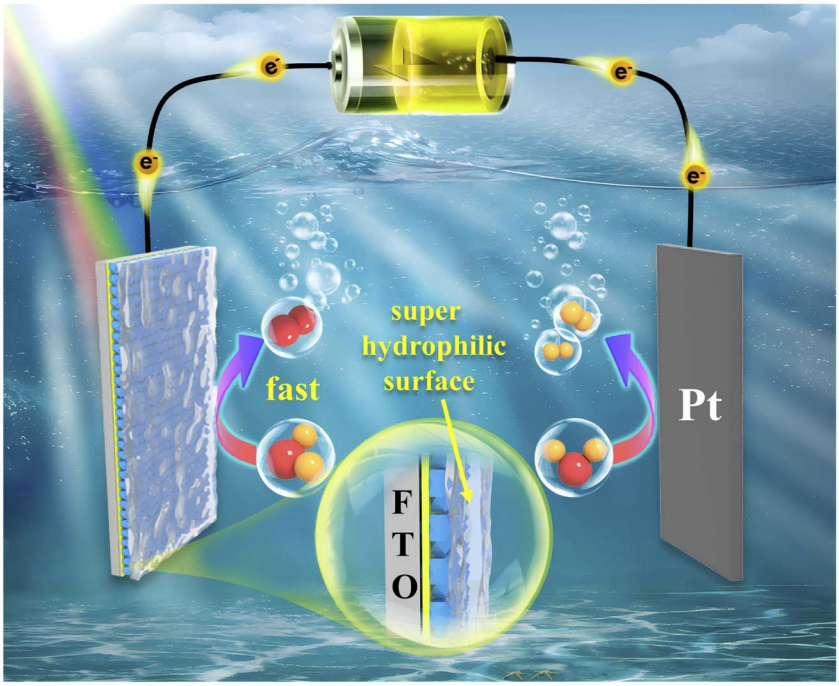

Scheme 2 The PEC water splitting mechanism diagram of the BVO@CoPc-S photoanode.

time-dependent, initial, and constant photocurrents, respectively. As shown in Fig. S2b,† the calculated τ values of BVO, BVO@CoPc-Dc, BVO@CoPc-I, and BVO@CoPc-S are 16 s, 62 s, 47 s, and 84 s, respectively. It suggests restricted charge recombination of BVO@CoPc-S photoanode, which may contribute to the rapid charge transfer with the good interface contact between CoPc and BVO. Stability is a vital element in assessing the PEC activity of photoanodes. As shown in Fig. 4e, pure BVO suffers a severe photocurrent loss with a decrease of 78% after 30 min. With the CoPc loading with various strategies, the photocurrent loss has been greatly reduced. BVO@CoPc-S displays only 27% decrease compared with the initial current density, outperforming that of BVO@CoPc-Dc (60%) and BVO@CoPc-I (37%). The good stability of BVO@CoPc-S may be ascribed to the strong interface contact between BVO and CoPc.

As shown in Fig. 4f, open-circuit potential (OCP) differences of BVO, BVO@CoPc-Dc, BVO@CoPc-I, and BVO@CoPc-S between dark and light conditions are 0.293 V, 0.382 V, 0.386 V, and 0.561 V, respectively. The enlarged OCP difference suggests the inhibited charge recombination. Additionally, the photovoltage of BVO@CoPc-S (0.28 V) is 260 mV, 170 mV, and 176 mV higher than that of BVO, BVO@CoPc-Dc, and BVO@CoPc-I, respectively. The accelerated charge transfer dynamics at the photoanode/electrolyte interface is reflected in the higher photovoltage of BVO@CoPc-S. In this work, Na_2SO_3 is used as the hole sacrificial agent to trap photogenerated holes. The charge injection efficiency (η_{inj}) of these photoanodes is measured as shown in Fig. 4g. At 1.23 V_{RHE}, BVO@CoPc-S shows higher η_{inj} values (58%) than that of BVO (18%), BVO@CoPc-Dc (38%) and BVO@CoPc-I (39%). This suggests that a higher quantity of holes at the photoanode/electrolyte interface contribute to the water oxidation reaction. The improved η_{inj} can attributed to the accelerated electron transfer and reduced charge recombination, thereby facilitating the water oxidation kinetics.

To further investigate the charge behavior at the photoanode/electrolyte interface, electrochemical impedance spectroscopy (EIS) was employed under light illumination. Fig. 4h shows the Nyquist curve and the fitted equivalent circuit model. R_s indicates the series resistance including FTO resistance and contact resistance, while the charge transfer resistance at the interface is represented by R_{ct}. The R_s values of BVO, BVO@CoPc-Dc, BVO@CoPc-I and BVO@CoPc-S are 20.1 Ω, 25.7 Ω, 26.2 Ω and 23.4 Ω, respectively. This result represents the negligible effect of CoPc loading with different load strategies on the R_s. Meanwhile, the R_{ct} values of BVO, BVO@CoPc-Dc, BVO@CoPc-I, and BVO@CoPc-S are 831.6 Ω, 213.4 Ω, 203.4 Ω and 122.5 Ω, respectively. A smaller arc radius generally indicates a faster charge transfer. BVO@CoPc-S exhibits the smallest radius and the lowest R_{ct} value, indicating the facilitated charge transfer at the photoanode/electrolyte interface.

The Mott–Schottky (M–S) curves for the prepared photoanodes are shown in Fig. 4i. These photoanodes display positive slopes, suggesting the n-semiconductor characteristics. In addition, the carrier density of the photoanode can be determined from Mott–Schottky plots using the following equation:

$$N_d = (2/e_0\varepsilon\varepsilon_0)[d(1/C^2)/dV]^{-1} \quad (2)$$

where e_0 is the electronic charge, ε is the dielectric constant of semiconductor, ε_0 is the dielectric constant of the vacuum, V is the bias voltage applied to the electrodes, and N_d is the donor

density. The N_d values of BVO, BVO@CoPc-Dc, BVO@CoPc-I and BVO@CoPc-S can be calculated as 0.8×10^{18} cm^{-3}, 1.1×10^{18} cm^{-3}, 1.2×10^{18} cm^{-3} and 2.3×10^{18} cm^{-3}, respectively. The increased carrier density indicates improved conductivity. This is consistent with the EIS analysis of BVO@CoPc-S.

On the basis of the aforementioned measurements and analysis, the PEC water-splitting mechanism of BVO@CoPc-S is proposed (Scheme 2). At first, the generation and separation of the electron–hole pairs occurs under illumination. Due to CoPc modification, photogenerated holes migrate to CoPc and participate in the water oxidation reaction. In addition, CoPc could provide the active site as a co-catalyst, which facilitated the water oxidation kinetics. Meanwhile, the hydrophilic surface of BVO@CoPc-S affords nice penetration and diffusion of the electrolyte, indeed promoting water oxidation. This good photoanode/electrolyte interface allows the generated holes to quickly participate in water oxidation, accelerates water oxidation kinetics and boosts the water splitting efficiency of PEC.

3. Conclusions

To sum up, super-hydrophilic BVO@CoPc-S composite photoanode was successfully prepared *via* a solvothermal treatment method. BVO@CoPc-S photoanode attained a remarkable photocurrent density of 4.0 mA cm^{-2} at 1.23 V_{RHE} and the maximum ABPE of 1.3% at 0.64 V_{RHE}. The exceptional PEC performance can be ascribed to the introduction of CoPc with providing active sites and super-hydrophilicity accelerating electrolyte diffusion. Benefit from this, the electrode can better match the electrolyte interface, which contribute to photogenerated carriers to be more efficiently injected into the electrolyte, effectively suppresses the recombination of bulk surface charges, and thus accelerates the surface reaction kinetics. Our work based on hydrophilic interfacial engineering provides valuable insights for designing and developing advanced hybrid photoanode structures for efficient PEC water splitting.

Data availability

All data are available in the ESI† and within the main manuscript.

Conflicts of interest

The authors declare no conflicts of interest.

Acknowledgements

This work is financially supported by the National Natural Science Foundation of China (Grant No. 22269002), Natural Science Foundation of Guangxi Province (Grant No. 2023GXNSFBA026182), and the Open Research Fund of Songshan Lake Materials Laboratory (Grant No. 2022SLABFN08).

References

1 R. T. Gao, D. He, L. J. Wu, K. Hu, X. H. Liu, Y. G. Su and L. Wang, *Angew. Chem., Int. Ed.*, 2020, **59**, 6213–6218.
2 V. O. Smilyk, S. S. Fomanyuk, I. A. Rusetskyi, M. O. Danilov and G. Y. Kolbasov, *Monatsh. Chem.*, 2024, **155**, 319–323.
3 H. Wu, L. Zhang, A. J. Du, R. Irani, R. van de Krol, F. F. Abdi and Y. H. Ng, *Nat. Commun.*, 2022, **13**, 6231.
4 J. Arun, S. Nachiappan, G. Rangarajan, R. P. Alagappan, K. P. Gopinath and E. Lichtfouse, *Environ. Chem. Lett.*, 2023, **21**, 339–362.
5 A. Fujishima and K. Honda, *Nature*, 1972, **238**, 37–38.
6 S. Lardhi, L. Cavallo and M. Harb, *J. Phys. Chem. Lett.*, 2020, **11**, 5497–5503.
7 A. Yamakata, C. S. K. Ranasinghe, N. Hayashi, K. Kato and J. J. M. Vequizo, *ACS Appl. Energy Mater.*, 2020, **3**, 1207–1214.
8 Y. H. Guo, Y. Q. Wu, Z. Q. Wang, D. J. Dai, X. L. Liu, Q. Q. Zhang, Z. Y. Wang, Y. Y. Liu, Z. K. Zheng, H. F. Cheng, B. B. Huang, Y. Dai and P. Wang, *Appl. Surf. Sci.*, 2023, **614**, 156164.
9 Y. R. Song, X. M. Zhang, Y. X. Zhang, P. L. Zhai, Z. W. Li, D. F. Jin, J. Q. Cao, C. Wang, B. Zhang, J. F. Gao, L. C. Sun and J. G. Hou, *Angew. Chem., Int. Ed.*, 2022, **61**, e202200946.
10 Z. Y. Tao, J. W. Yang, Y. Wu, Q. Zhao, J. P. Li and G. Liu, *Int. J. Hydrogen Energy*, 2024, **61**, 851–858.
11 Z. M. Zhou, J. J. Chen, Q. L. Wang, X. X. Jiang and Y. Shen, *Chin. J. Catal.*, 2022, **43**, 433–441.
12 D. M. Chen, X. L. Li, J. Y. Huang, Y. X. Chen, Z. L. Liu and Y. C. Huang, *ACS Appl. Energy Mater.*, 2023, **6**, 8495–8502.
13 Y. P. Li, H. Han, A. D. Xu, Y. M. Fu, C. F. Zhu, L. J. Cheng and Y. G. Li, *Inorg. Chem.*, 2023, **62**, 17851–17860.
14 J. C. Wang, Y. Zhang, J. Bai, J. H. Li, C. H. Zhou, L. Li, C. Y. Xie, T. S. Zhou, H. Zhu and B. X. Zhou, *J. Colloid Interface Sci.*, 2023, **644**, 509–518.
15 M. R. Wang, Z. Y. Wang, B. Zhang, W. Y. Jiang, X. L. Bao, H. F. Cheng, Z. K. Zheng, P. Wang, Y. Y. Liu, M. H. Whangbo, Y. J. Li, Y. Dai and B. B. Huang, *ACS Catal.*, 2020, **10**, 13031–13039.
16 G. Q. Liu, F. Li, Y. Zhu, J. Y. Li and L. C. Sun, *RSC Adv.*, 2020, **10**, 28523–28526.
17 J. Zuo, H. L. Guo, S. Chen, Y. Pei and C. J. Liu, *Catal. Sci. Technol.*, 2023, **13**, 3963–3973.
18 X. K. Wan, G. Z. Liu, X. Y. Wang, D. S. Lu, Y. M. Fu, X. J. Guan, C. Hu, N. Rong and H. T. Wang, *J. Photochem. Photobiol., A*, 2024, **451**, 115527.
19 Z. J. Sun, C. W. Xu, Z. Li, F. Guo, B. S. Liu, J. H. Liu, J. Zhou, Z. Q. Yu, X. He and D. C. Jiang, *New J. Chem.*, 2022, **46**, 9111–9118.
20 X. L. Shen, L. Zhao, W. Q. Fan, J. S. Ren, Q. Wang, A. J. Wang, D. H. Shang and W. H. Zhu, *Appl. Surf. Sci.*, 2021, **564**, 150463.
21 M. M. Fan, Z. Y. Tao, Q. Zhao, J. P. Li, G. Liu and C. Zhao, *Adv. Mater. Technol.*, 2023, **8**, 2201835.
22 Z. Cai, Y. S. Zhang, Y. X. Zhao, Y. S. Wu, W. W. Xu, X. M. Wen, Y. Zhong, Y. Zhang, W. Liu, H. L. Wang, Y. Kuang and X. M. Sun, *Nano Res.*, 2019, **12**, 345–349.

23 S. S. Chen, S. Shen, G. J. Liu, Y. Qi, F. X. Zhang and C. Li, *Angew. Chem., Int. Ed.*, 2015, **54**, 3047–3051.
24 T. T. Zhang, P. Lin, N. Wei and D. A. Wang, *ACS Appl. Mater. Interfaces*, 2020, **12**, 20110–20118.
25 P. F. Yue, H. D. She, L. Zhang, B. Niu, R. Lian, J. W. Huang, L. Wang and Q. Z. Wang, *Appl. Catal., B*, 2021, **286**, 119875.
26 Y. B. Kuang, T. Yamada and K. Domen, *Joule*, 2017, **1**, 290–305.
27 P. Mane, I. V. Bagal, H. Bae, V. Burungale, C. Seong, S. W. Ryu and J. S. Ha, *Adv. Sustainable Syst.*, 2022, **6**, 2200014.
28 T. W. Kim and K. S. Choi, *Science*, 2014, **343**, 990–994.
29 J. B. Pan, B. H. Wang, S. Shen, L. Chen and S. F. Yin, *Angew. Chem., Int. Ed.*, 2023, **62**, e202307246.
30 Z. X. Liu, F. Y. Zhao, X. H. Liu, Y. H. Fu, Y. Song, P. Y. Wang, X. X. Zhang, G. W. Wang and H. C. Ma, *Langmuir*, 2024, **40**, 1348–1357.
31 S. C. Wang, P. Chen, J. H. Yun, Y. X. Hu and L. Z. Wang, *Angew. Chem., Int. Ed.*, 2017, **56**, 8500–8504.
32 R. L. Wang, Y. Kuwahara, K. Mori, C. Louis, Y. Y. Bu and H. Yamashita, *J. Mater. Chem. A*, 2020, **8**, 21613–21622.
33 K. S. Joya, N. Morlanés, E. Maloney, V. Rodionov and K. Takanabe, *Chem. Commun.*, 2015, **51**, 13481–13484.
34 Y. D. Liu, Y. Jiang, F. Li, F. S. Yu, W. C. Jiang and L. X. Xia, *J. Mater. Chem. A*, 2018, **6**, 10761–10768.
35 G. S. Liu, S. W. Liu, Q. F. Lu, H. Y. Sun and Z. L. Xiu, *RSC Adv.*, 2014, **4**, 53402–53406.
36 M. Y. Zhang, C. L. Shao, Z. C. Guo, Z. Y. Zhang, J. B. Mu, T. P. Cao and Y. C. Liu, *ACS Appl. Mater. Interfaces*, 2011, **3**, 369–377.
37 Z. Y. Long, X. Y. Zheng and H. F. Shi, *Sci. China Mater.*, 2024, **67**, 550–561.
38 D. C. Jiang, L. Zhang, Q. D. Yue, T. T. Wang, Q. Huang and P. W. Du, *Int. J. Hydrogen Energy*, 2021, **46**, 15517–15525.
39 J. Choi, P. Wagner, S. Gambhir, R. Jalili, D. R. MacFarlane, G. G. Wallace and D. L. Officer, *ACS Energy Lett.*, 2019, **4**, 666–672.
40 X. S. Hu, Q. Z. Wang, Y. Li, Y. Meng, L. Wang, H. D. She and J. W. Huang, *J. Colloid Interface Sci.*, 2022, **607**, 219–228.
41 O. L. Li, L. Qin, N. Takeuchi, K. Kim and T. Ishizaki, *Catal. Today*, 2019, **337**, 155–161.
42 W. H. Xie, Z. B. Yu, H. C. Huang, R. H. Jiang, S. Q. Yao, J. Huang, Y. P. Hou, S. B. Yin, R. L. Mo and C. Wu, *J. Colloid Interface Sci.*, 2024, **665**, 977–987.
43 S. P. Wan, C. R. Dong, J. Jin, J. Li, Q. Zhong, K. Zhang and J. H. Park, *ACS Energy Lett.*, 2022, **7**, 3024–3031.